ARMY RESEARCH LABORATORY

A New Helicopter Transmission Model for Condition-based Maintenance Technologies Using First Principles

by David B. Stringer, Pradip N. Sheth, and Paul E. Allaire

ARL-TR-4984 **September 2009**

NOTICES

Disclaimers

The findings in this report are not to be construed as an official Department of the Army position unless so designated by other authorized documents.

Citation of manufacturer's or trade names does not constitute an official endorsement or approval of the use thereof.

DESTRUCTION NOTICE—For classified documents, follow the procedures in DoD 5220.22-M, National Industrial Security Program Operating Manual, Chapter 5, Section 7, or DOD 5200.1-R, Information Security Program Regulation, C6.7. For unclassified, limited documents, destroy by any method that will prevent disclosure of contents or reconstruction of the document.

Army Research Laboratory
Cleveland, Ohio 44135

ARL-TR-4984 **September 2009**

A New Helicopter Transmission Model for Condition-based Maintenance Technologies Using First Principles

David B. Stringer
Vehicles Technology Directorate, ARL

Pradip N. Sheth and Paul E. Allaire
University of Virginia, Charlottesville, Virginia, 22904

REPORT DOCUMENTATION PAGE	Form Approved OMB No. 0704-0188

1. REPORT DATE *(DD-MM-YYYY)*	2. REPORT TYPE	3. DATES COVERED (From - To)
September 2009		

4. TITLE AND SUBTITLE

A New Helicopter Transmission Model for Condition-based Maintenance Technologies Using First Principles

5a. CONTRACT NUMBER

5b. GRANT NUMBER

5c. PROGRAM ELEMENT NUMBER

6. AUTHOR(S)

David B. Stringer, Pradip N. Sheth, and Paul E. Allaire

5d. PROJECT NUMBER

5e. TASK NUMBER

5f. WORK UNIT NUMBER

7. PERFORMING ORGANIZATION NAME(S) AND ADDRESS(ES)

U.S. Army Research Laboratory
ATTN: RDRL-VT
Cleveland, Ohio, 44135

8. PERFORMING ORGANIZATION REPORT NUMBER

ARL-TR-4984

9. SPONSORING/MONITORING AGENCY NAME(S) AND ADDRESS(ES)

10. SPONSOR/MONITOR'S ACRONYM(S)

11. SPONSOR/MONITOR'S REPORT NUMBER(S)

12. DISTRIBUTION/AVAILABILITY STATEMENT

Approved for public release; distribution unlimited.

13. SUPPLEMENTARY NOTES

14. ABSTRACT

This report presents a new helicopter transmission model in support of condition-based maintenance (CBM) initiatives. The model uses the first principles approach to analyze the rotating shafts and gear couplings using rotor dynamic analysis techniques. The helicopter transmission is presented, followed by a discussion of the finite element formulation to include gear mesh modeling methodologies. System natural frequencies and mode shapes are discussed, along with the model's validation procedure. The model's primary purpose is to simulate multiple operating conditions to include faults. One such fault condition simulates the wear of gear tooth contact surfaces. The nature of the fault and its modeling techniques are discussed. Simulation results are presented in the time domain using a conventional vibration diagnostic parameter. A new diagnostic parameter, the FE2, is also introduced for detecting faults in the frequency domain. Additional considerations and further research points are also discussed. The results demonstrate the potential of physics-based, mathematical models in providing a key technology enabler for improving health monitoring and prediction capabilities of CBM strategies.

15. SUBJECT TERMS

Thermal, simulation, silicon carbide, power

16. SECURITY CLASSIFICATION OF:			17. LIMITATION OF ABSTRACT	18. NUMBER OF PAGES	19a. NAME OF RESPONSIBLE PERSON
a. REPORT	b. ABSTRACT	c. THIS PAGE	UU	30	David B. Stringer
Unclassified	Unclassified	Unclassified			19b. TELEPHONE NUMBER (*Include area code*) (216) 433-8482

Contents

List of Figures

List of Tables

Acknowledgments

Dr. Dave Lewicki and Dr. Brian Dykas of the Army Research Lab's Vehicle Technology Directorate, Cleveland, Ohio, were particularly helpful in providing test data, transmission information, and assistance in testing set-up on ARL/NASA's 500 hp Transmission Test Stand.

INTENTIONALLY LEFT BLANK

1. Introduction

The paradigm shift to condition-based maintenance (CBM) of vertical lift aircraft requires advanced methods of health and condition monitoring, characterized by high detection rates and low false alarms, using recorded signals from sensors placed at key locations throughout the aircraft. Furthermore, not only must the condition monitoring equipment detect any faults, it should also determine which component has those faults based upon the physical signature. A key technology enabler is a fast, reliable source of information to compare against real-time or near real-time aircraft data. This capability requires a database of operating conditions, simulating both normal and abnormal operations. Ultimately, it requires a method of modeling the dynamics of the system.

This is particularly relevant in rotorcraft drive trains. Helicopters rely on the integrity of their drive train(s) for their airworthiness and autorotational capability. Indeed, drive system emergencies represent the most critical in-flight emergency, after fire, in many rotary-wing platforms. A study of civilian rotorcraft accidents between 1960 and 1997 concluded that transmission malfunctions caused or contributed to approximately 13 accidents per year (*1*). This was most recently reiterated in a recent accident off the coast of Scotland, caused by the catastrophic failure of the aircraft's main rotor gearbox (*2*).

Physics-based models are an acknowledged shortcoming in rotorcraft health monitoring and diagnostic methodologies (*3*). The current state-of-the-art is characterized by an overwhelming focus on experimental testing of faults, fault seeding, and detection methodologies using vibration signatures and condition indicators (CIs). The literature groups current research into the following loose classifications: (1) stochastic and statistical detection methodologies (*4–8*), (2) empirical testing and results (*9–11*), (3) condition indicators, threshold values, algorithms, and algorithm effectiveness (*12–16*), (4) the types of faults (*17–25*), and (5) vibration signatures and signal processing (*26–35*). These classifications are not meant to provide rigid divisions in the research; indeed, some research crosses into two or more of these classifications.

The overarching enabler of transmission effectiveness is gear technology. Drive trains rely on gear quality and health for their integrity and function. The dynamics associated with geared motion are complex. Gears greatly influence the vibration characteristics of a mechanical system and contribute significantly to the noise, component fatigue, and personal discomfort prevalent in rotorcraft.

The dynamic analysis of gears dates back to the 1950s. Models of various gear-mesh interactions permeate the literature (*36, 37*). By and large, these studies dealt with dual shafts coupled by a single gear pair, or multiples shafts coupled by gear pairs using the same types of gears, i.e., spur, helical, bevel, etc.

What has not been adequately captured, however, is the dynamic modeling of a helicopter or gearbox consisting of multiple shafts connected by multiple gears of different configurations. With the exception of one study in the late 1980's (*38*), work in this area has been relatively overlooked. The complexity of the transmission dynamics and transmission paths has traditionally made extraction and interpretation of fault detection data difficult (*39*). However, interest in physics-based models has increased in recent years, specifically in terms of predicting the noise path through a rotorcraft transmission (*40*).

This report presents a finite element model of a helicopter transmission in support of health monitoring, diagnostics, and other CBM initiatives. It includes a detailed description of the model and system parameters, method of validation, summary of results simulating both normal and abnormal operating conditions, and finally, a demonstration of fault detection capability using both a conventional and a new diagnostic parameter.

2. OH-58 Helicopter and Transmission

The model configuration is based upon the 500 hp Transmission Stand jointly used by the Army and NASA at the NASA Glenn Research Center in Cleveland, Ohio. The OH-58 helicopter is a single-engine, light helicopter used for observation and reconnaissance. More recognizable are its civilian counterparts, the Bell 406, which are familiar to most as news and traffic helicopters reporting over major metropolitan areas in the United States. The current transmission mounted in the stand belonged to the C-model aircraft. The stand has also tested the A-model transmission (*10*). The D-model is the most current platform in use by the Army.

The OH-58 transmission provides speed and torque reduction through two stages. The first stage consists of a spiral-bevel configuration. The near-horizontal input shaft holds a 19-tooth spiral-bevel pinion which drives a 71-tooth spiral-bevel gear on a near-vertical intermediate shaft. The directional change in shaft rotation totals 94 degrees and occurs in this first stage.

The second stage uses a planetary gear configuration. The intermediate shaft from the first stage also contains a 27-tooth sun gear. The sun gear drives three or four 35-planet planetary gears, depending upon aircraft model. The planets mesh with a stationary 99-tooth ring gear splined to the top of the transmission casing. The rotating planet gears drive the carrier, which is attached to the output shaft. The output shaft rests within the intermediate shaft. Various roller and ball bearings hold the shafts and planets in place. The total reduction ratio is 17.44:1. Figure 1 depicts the transmission of the A-model aircraft.

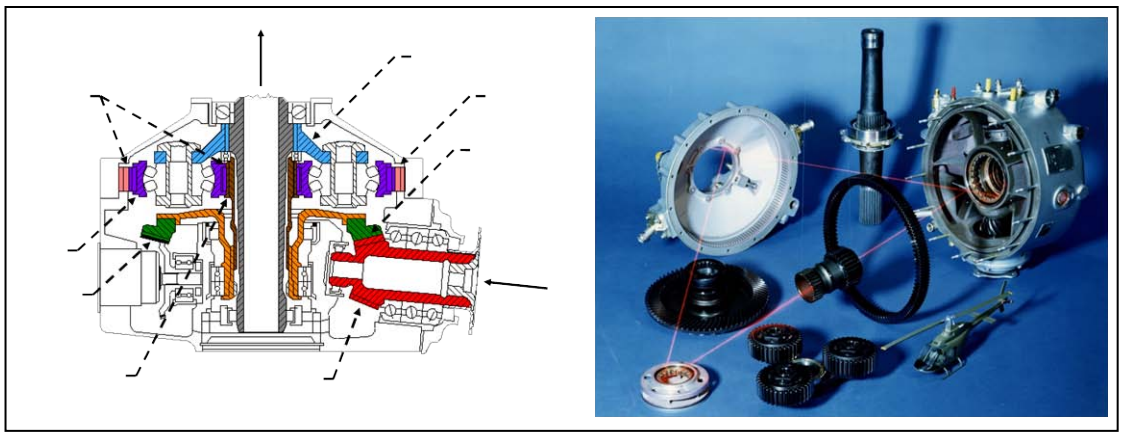

Figure 1. OH-58 transmission schematic (left) and disassembled (right).

3. Transmission Model

3.1 Description and Model Assembly

The model uses a lumped parameter, finite element formulation of the familiar equations of motion.

$$[\mathbf{M}]\{\ddot{\mathbf{q}}\}+[\mathbf{C}]\{\dot{\mathbf{q}}\}+[\mathbf{G}]\{\dot{\mathbf{q}}\}+[\mathbf{K}]\{\mathbf{q}\}=\{\mathbf{F}(t)\} \tag{1}$$

The subcomponents of the model consist of the three shafts, the stationary ring gear, and the planet gears. In other words, these five subcomponents have their own matrix elements for satisfying equation 1 above (*41*). The spiral-bevel pinion, spiral-bevel gear, sun gear, and planet carrier are assumed to be point masses acting at the appropriate nodes along their respective shaft. The ring and planet gears also act as point masses at independent nodes not associated with any shaft. The input, intermediate, and output shafts are designated as Shafts A, B, and C, respectively.

Coupling of subcomponents occurs through gear-mesh interactions. The model interprets these interactions as linear stiffness matrices. While gear loading itself is inherently nonlinear, the model maintains the nonlinearities on the right hand side of equation 1 as forcing functions. Although a nonlinear model is possible with minor modifications, the linear treatment is maintained for ease of analysis.

Many gear-mesh formulations are available in the literature. However, the fundamental characteristic of the spiral-bevel mesh matrix used here is its twelve degrees-of-freedom (dof's), corresponding to each of the six dof's at the two coupling nodes. Although spiral-bevel gear geometry and force transfer are some of the most complex in the gearing industry, two

approaches have been used in this model. The first uses the method of Tregold's Approximation, modeling the two spiral-bevel gears as equivalent spur gear sets (*42*). This assumption enables the use of a 12-dof spur and helical gear mesh matrix (*43*). The second and more accurate approach rigorously develops the mesh matrix based upon vector calculus of the gear geometry (*44*). Both techniques have been used with comparable results. The results presented here use the more rigorous mesh matrix development.

The epicyclic stage of the transmission is more complex due to its multiple components and the orbital motion of the planets. For convenience, the system model implements an existing lumped parameter epicyclic model from the literature (*45, 46*). Each subcomponent is placed at its appropriate shaft node in the model as discussed previously.

Figure 2 presents a comprehensive illustration of the transmission model by subcomponent. The nodes on the three shafts each have the conventional six dof's. The nodes of each shaft were placed at key locations as dictated by shaft geometries, gear-mesh, and bearing locations. Shafts A and B each have eight nodes. Shaft C consists of 13 nodes. The total number of dof's for the shafts is 174. The epicyclic components each have three dof's – two in translation and one in rotation (torsional). The ring and planets therefore total 3+3*n* dof's, where *n* is the number of planet gears. The carrier and sun gear also contain three dof's, which are expanded into the traditional 6-dof matrix at their respective nodes. The total number of dof's in the model is 177+3*n*.

Some final comments regarding the model setup. Note that each shaft has a non-uniform cross sectional area. The model assumes an equivalent cross-sectional area for the inner and outer diameters of each shaft. It neglects transmission error within the gear meshes. Lastly, the transmission casing itself is neglected in this analysis. The system parameters follow in table 1.

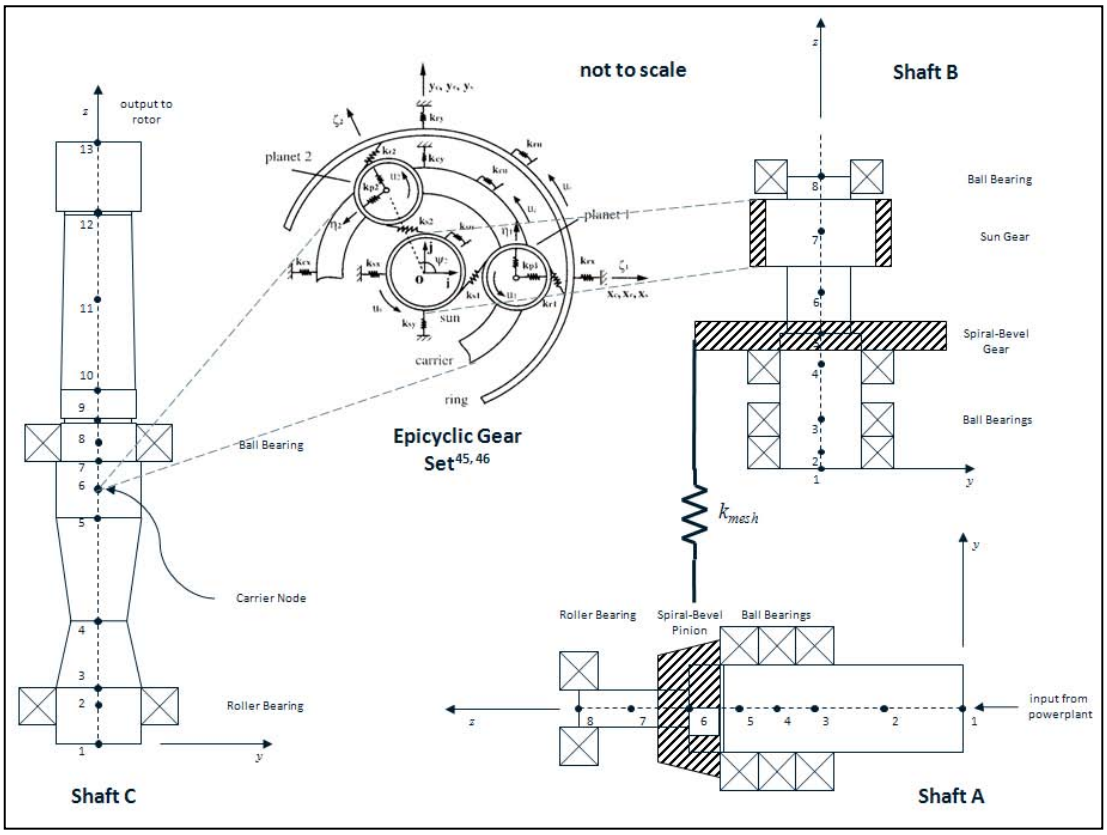

Figure 2. Finite element model component layout.

Table 1. Transmission model parameters.

Material Parameters		**Shaft A: Input Shaft**	
Young's Modulus (E) (N/m^2)	2.05E11	Length (m)	0.150
Shear Modulus (G) (N/m^2)	8.0E10	Outer Diameter (eq) (d_{so}) (m)	0.050
Poisson's Ratio (□)	0.29	Inner Diameter (eq) (d_{si}) (m)	0.033
Density (□) (kg/m^3)	7850		
Shaft B: Intermediate Shaft		**Shaft C: Mast Output Shaft**	
Length (m)	0.154	Length (m)	0.460
Outer Diameter (eq) (d_{so}) (m)	0.073	Outer Diameter (eq) (d_{so}) (m)	0.057
Inner Diameter (eq) (d_{si}) (m)	0.058	Inner Diameter (eq) (d_{si}) (m)	0.021
Spiral-Bevel Pinion (Shaft A)		**Spiral-Bevel Gear (Shaft B)**	
Mass (kg)	0.47	Mass (kg)	2.24
Moment of Inertia (I_t) ($kg\ m^2$)	1.4E-4	Moment of Inertia (I_t) ($kg\ m^2$)	1.5E-4
Polar Moment of Inertia (I_p) ($kg\ m^2$)	2.8E-4	Polar Moment of Inertia (I_p) ($kg\ m^2$)	3.0E-4
Diameter (d_g) (m)	0.062	Diameter (d_g) (m)	0.228
Pitch Angle (Γ) (deg)	15.3	Pitch Angle (Γ) (deg)	78.7
Pressure Angle (α_n) (deg)	20	Pressure Angle (α_n) (deg)	20
Spiral Angle (ψ) (deg)	30.0	Spiral Angle (ψ) (deg)	30.0
Orientation Angle (φ) (deg)	0.0	Orientation Angle (φ) (deg)	0.0
Average Mesh Stiffness (K_g) (N/m)	1.0E8	Average Mesh Stiffness (K_g) (N/m)	1.0E8
Number of Teeth	19	Number of Teeth	71
Carrier		**Sun**	
Mass (kg)	5.43	Mass (kg)	0.40
Moment of Inertia (I_t) ($kg\ m^2$)	0.0492	Moment of Inertia (I_t) ($kg\ m^2$)	5.841E-4
Diameter (d_g) (m)	0.1768	Diameter (d_g) (m)	0.0774
Pressure Angle (α_n) (deg)	20	Pressure Angle (α_s) (deg)	24.6
Bearing Stiffness (k_{bc}) (N/m)	1.0E8	Bearing Stiffness (k_{bs}) (N/m)	1.0E8
Torsional Bearing Stiffness (k_{cu}) ($N\text{-}m/rad$)	100	Torsional Bearing Stiffness (k_{su}) ($N\text{-}m/rad$)	100
		Number of Teeth	27
Ring		**Planet**	
Mass (kg)	2.35	Number of Planets	4
Moment of Inertia (I_t) ($kg\ m^2$)	0.0567	Mass (kg)	0.66
Diameter (d_g) (m)	0.275	Moment of Inertia (I_t) ($kg\ m^2$)	0.0015
Pressure Angle (α_r) (deg)	24.6	Diameter (d_g) (m)	0.1003
Bearing Stiffness (k_{br}) (N/m)	1.0E15	Pressure Angle (α_n) (deg)	20
Torsional Bearing Stiffness (k_{ru}) ($N\text{-}m/rad$)	1.0E15	Bearing Stiffness (k_{br}) (N/m)	1.0E8
Number of Teeth	99	Number of Teeth	35
Duplex, Triplex, and Roller Bearing			
k_{xx}, k_{yy} (N/m)	1.0E9		

3.2 Simulation Setup

The basic function of the model is to provide a response to a given set of inputs, such that the output approximates experimental results. These inputs represent both normal and abnormal

operating conditions. The inputs are modeled by forcing functions on the right hand side of equation 1. It is here that gear dynamics become readily apparent. The dynamics of the spiral-bevel and gear-mesh frequencies and their harmonics dominate the transmission response (*10*). This is most easily illustrated by a data sample from the OH-58 Transmission Test Stand. The test conditions were an input speed of 6060 rpm, torque of 350.1 N-m, and full mast loading. Figure 3 depicts the response from an accelerometer near the ring gear at the left trunnion mount. The gear-mesh frequency harmonics of both gear stages are identified.

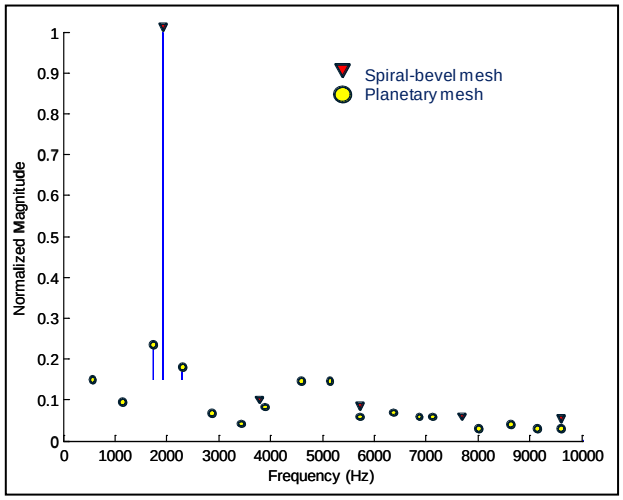

Figure 3. Sample data from OH-58 transmission test stand.

The data in figure 3 show 22 total gear-mesh harmonics for the OH-58C transmission in the spectrum between 0 and 10,000 Hz, clearly illustrating the gear-mesh contributions to the overall dynamics of the system. This significantly contributes to the complexity of the modeling problem, since each harmonic represents an individual model input. This leads to another dilemma, specifically, how to determine the amplitudes of the respective forcing functions, since no closed form methodology exists. Similarly, the gear-mesh contributions also result in sideband frequencies, which must be addressed as they have also been used to detect fault conditions (*47*).

In light of these considerations, the force vector of equation 1 must consist of several terms to accurately simulate the dynamics of the system. This may or may not be feasible, and the results must be closely scrutinized to determine the sensitivity of the model output to the inputs. A representative simulation equation therefore might resemble equation 2.

$$[\mathbf{M}]\{\ddot{\mathbf{q}}\}+[\mathbf{C}]\{\dot{\mathbf{q}}\}+[\mathbf{G}]\{\dot{\mathbf{q}}\}+[\mathbf{K}]\{\mathbf{q}\}=\{\mathbf{T}\}e^{j\Omega t}+\sum_{i=1}^{\infty}\{\mathbf{F}_b\}_i\, e^{j(i\cdot NT_b\cdot\Omega_b)t}+\sum_{i=1}^{\infty}\sum_{j=1}^{\infty}\{\mathbf{F}_{sb-b}\}_i\, e^{j(i\cdot NT_b\cdot\Omega_b\pm j\cdot\Omega_b)t}+\ldots \quad (2)$$

where the terms on the right hand side represent the torque vector, the spiral-bevel gear-mesh harmonics, and the spiral-bevel sideband harmonics, respectively. The ellipsis in equation 2

represents other multiple inputs required to model the system dynamics, such as the planetary gear-mesh harmonic contributions.

4. Model Validation

Preliminary model validation occurred by using traditional impact testing procedures to identify natural frequencies of the four-planet transmission configuration in the ARL/NASA Test Stand. Three accelerometers at different locations on the casing recorded the response from successive impacts at four different impact locations. Four impacts occurred at each location, resulting in 48 test samples. From this data, the experimental natural frequencies were extracted.

Figure 4 compares the model's natural frequencies (*x*-axis) determined from eigenvalue analysis to those frequencies identified from the experimental data (*y*-axis), and plots them with respect to the correlation line. The correlation line is the 45° dotted line representing an exact 1:1 comparison. In figure 4, note the close proximity of all predicted data points to the correlation line. Additionally, figure 4 identifies four bands of unpredicted frequencies. These represent frequencies measured during experimental testing with no corresponding prediction in the model. They were highlighted and placed on the correlation line. The current hypothesis suggests that they are frequencies associated with the transmission casing, which the model currently neglects. Future incorporation of the casing into the model will prove or disprove this hypothesis. Nevertheless, these results provide a significant level of confidence to the model in its current configuration.

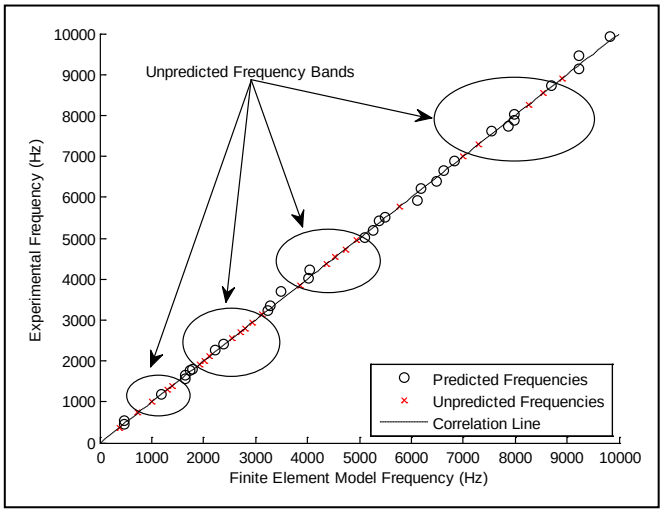

Figure 4. Experimental versus model frequency.

5. Eigen Analysis Results – Mode Shapes

Initial model analysis solved the eigenvalue problem of the undamped system, accounting for gyroscopic effects, using the traditional state-space formulation. Since gyroscopic effects are a function of rotational speed, the nominal speed of the input shaft was set at 6,060 rpm, matching the speed of the transmission input from the test environment and the aircraft (*10*).

The eigenvalues and eigenvectors represent the system natural frequencies and mode shapes, respectively, as a function of shaft operating speed. Since the frequencies have already been addressed, the mode shapes are the objectives of this discussion. Frequency variation with operating speed is not significant in this analysis and is neglected.

The lateral-torsional vibration coupling that occurs in mode shapes of geared systems has been well documented since the 1970s (*48*). Epicyclic mode shapes result in a different coupling and have also been characterized (*45, 46*). Figure 5 depicts the coupled mode shapes of the three shafts corresponding to a frequency of 3,230 Hz. The upper three charts show the lateral displacements of (a) Shaft A, (b) Shaft B, and (c) Shaft C. Likewise the lower three charts show the torsional displacement among the three shafts, respectively. The dotted vertical lines in the lower charts correspond to the location of the gear mesh at each shaft. In the case of Shaft C (figure 5.c), the vertical line corresponds to the location where the planet carrier connects to the mast output shaft.

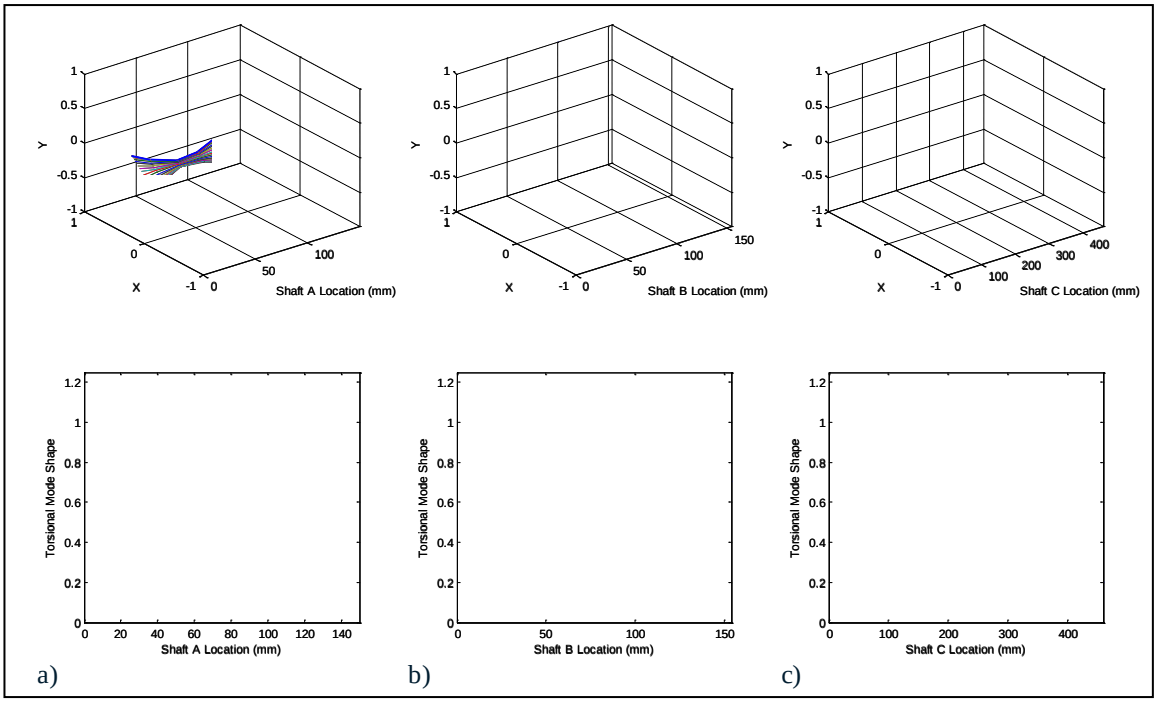

Figure 5. Shaft mode shapes –3,230 Hz.

Figure 5 illustrates the lateral-torsional mode coupling of the three shafts. The mode shapes are planar, another feature indicative of coupling (*43*). Although this study presents only one illustrative mode shape, it is worth mentioning that all observed lower mode shapes exhibited this same pattern, namely, coupled and planar. The mode shapes of the ring and planets have been omitted for brevity. However, these results illustrate the need for further study and classification of the mode shapes of such a complex system.

6. Dynamic Simulation Results with Fault Detection

The dynamic simulations examine two conditions. The first represents a transmission under "normal" operating conditions. The second condition seeds a fault in the spiral-bevel mesh, simulating gear-tooth surface wear. Wear is a gradual process, characterized by the mild deterioration of the mating surface due to sliding action between teeth. It can accelerate the likelihood of fatigue failures (*25)* and negatively impact other drive system components (*24*). Figure 6 shows a gear experiencing a worn condition.

Due to its gradual nature, the likelihood of serious damage from worn gears is quite low. Nevertheless, this fault was selected because it is one of the most overlooked faults (*23*), and it is also one of the easiest to model for demonstration purposes.

In the mathematical model, the wear condition is captured by an altered loading pattern within the gear-mesh (*23*). Such a pattern is presented in figure 7. The solid line represents a normal gear loading pattern. The dotted line simulates the worn condition. These loading conditions occur at the pitch point in the gear mesh. One will also note that due to the gradual process, wear affects more than one gear tooth simultaneously. The chart in figure 7 therefore implies that all gear teeth have undergone wear. This decreases the model complexity substantially.

The normal loading pattern of figure 7 is found using a conventional finite element, contact analysis solver. As such, these loading patterns do not exist in closed form. They must be approximated by curve fit. Afterwards, a transformation procedure converts them into the appropriate force vectors.

The first step in this simulation was to approximate a curve to the loading pattern representing normal operation of the spiral bevel gear mesh. The Fourier series of equation 3 is appropriate.

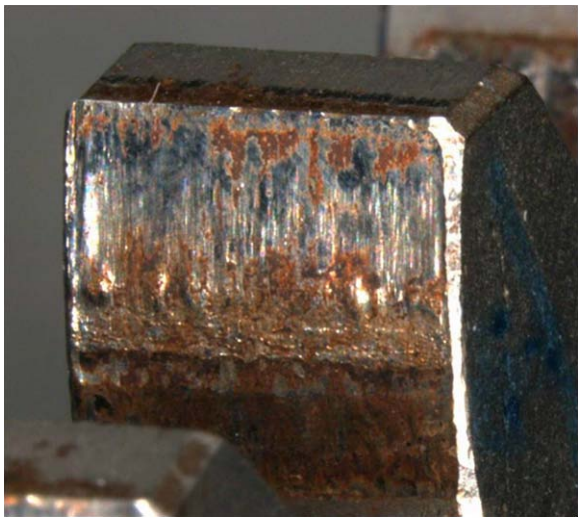

Figure 6. Gear tooth with wear.

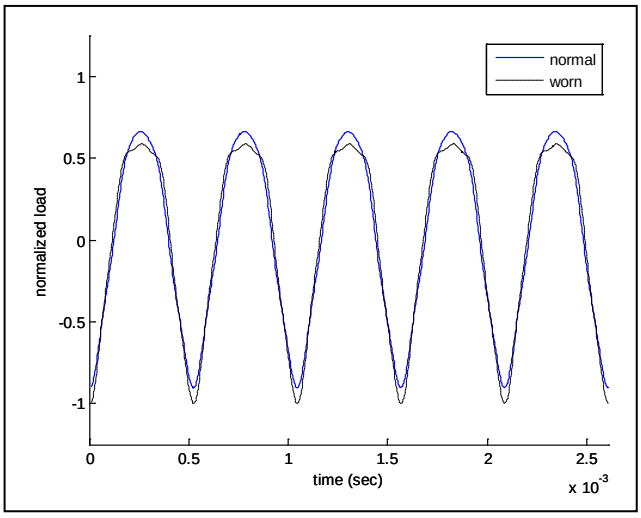

Figure 7. Spiral-bevel gear loading conditions.

$$\mathbf{F}(t) = \sum_{n=1}^{\infty} \{a\}_n \cos\left(n \cdot NT_b \cdot \Omega_b \cdot t\right) + \sum_{n=1}^{\infty} \{b\}_n \sin\left(n \cdot NT_b \cdot \Omega_b \cdot t\right) \tag{3}$$

Equation 3 represents the periodic loading of the gear teeth at harmonics of the spiral-bevel, gear-mesh frequency, ($n \cdot NT_b \cdot \Omega_b$), with the Fourier coefficients as the gear-mesh harmonic amplitudes. The input operating speed of 6,060 rpm (101 Hz) results in 5 gear-mesh harmonics between 0 and 10,000 Hz. The Fourier coefficients are then approximated by the curve-fit software. Table 2 provides the Fourier coefficients for both the normal and damage conditions used in figure 7. Finally, these loading patterns when resolved into two 6-dof force vectors, represent the forces and moments acting at the appropriate nodes on Shafts A and B.

Table 2. Loading pattern Fourier coefficients.

		normal			**worn**	
n		**a_n**	**b_n**		**a_n**	**b_n**
1		–402	–3.26		–402	–4.25
2		–49.04	–0.795		–100	–0.7
3		–2.44	–0.059		–2	–0.02
4		–15	–5		–9	–6
5		–10	–3		–15	–8

The system response was calculated for the force and moment vectors of each harmonic as indicated in equation 2. The superposition of these responses results in the total dynamic response. For this study, the forcing functions include only the force and moment vector of the applied torque, and the vectors of the spiral-bevel gear harmonics. It does not include any gear-mesh sidebands or planetary gear-mesh contributions. Figure 8 depicts the lateral response, measured at the input node of Shaft A, for both (a) normal and (b) worn conditions.

The difference in the two vibration patterns is clearly noticeable. However, the presence of this worn condition (figure 8.b) did not produce a drastic change in the vibration pattern. This is not unexpected, given the gradually progressive nature of the fault. This also indicates that the traditional vibration diagnostic parameters may not be effective in detecting this type of fault.

One such parameter is the signal kurtosis, presented in figure 9. It is a statistical measure, calculated from a sample of accelerometer signals. A normal signal condition returns a kurtosis value of approximately 3. A fault condition results in a higher value, with a threshold of 7 being a clear indicator of damage. Figure 9 shows the kurtosis value for a string of 2,048 data points. The first 1,024 data points have no fault. The second half of the data points represents the introduction of the fault condition. Figure 9 shows only a slight increase in the kurtosis value. Although the increase is detectable, it does not come near the threshold value. Another method of fault detection is necessary for this condition.

The frequency domain provides such an alternative. Using the FFT algorithm, the model provided both responses in the frequency domain, presented in figure 10. The differences

between the two conditions are readily apparent. Quantifying these differences resulted in the development of a simple metric, designated FE2. In the most basic of terms, the FE2 is the square of the percentage error between frequency signals, defined by equation 4. The square in equation 4 increases the detection of faults by eliminating smaller peaks (<1), while magnifying larger peaks.

$$FE2 = \left[100 \cdot \left(\frac{s_{damage} - s_{normal}}{s_{normal}} \right) \right]^2 \tag{4}$$

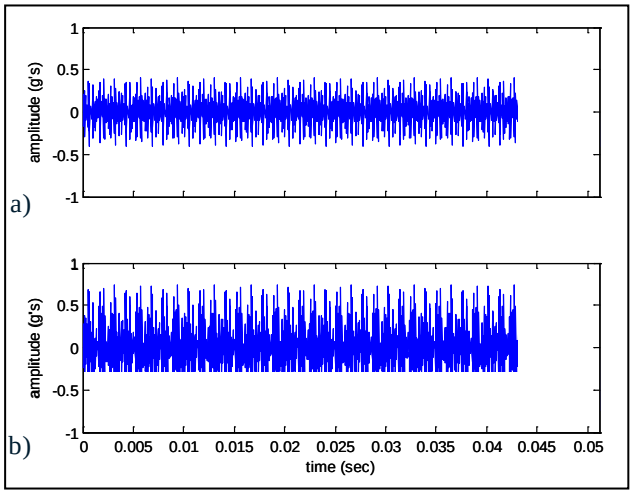

Figure 8. (a) Normal and (b) worn vibration response.

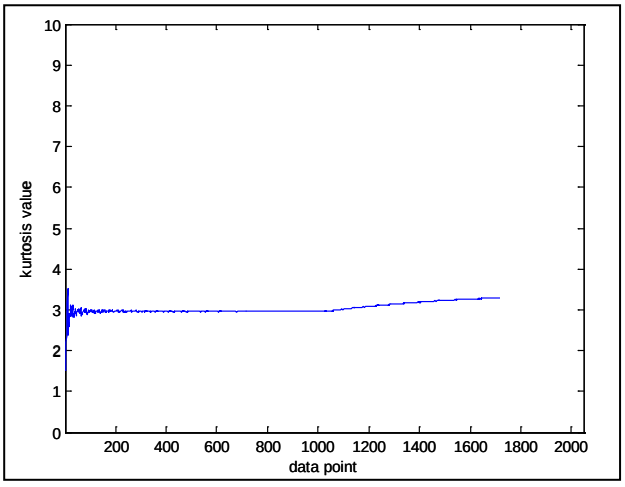

Figure 9. Kurtosis diagnostic parameter results.

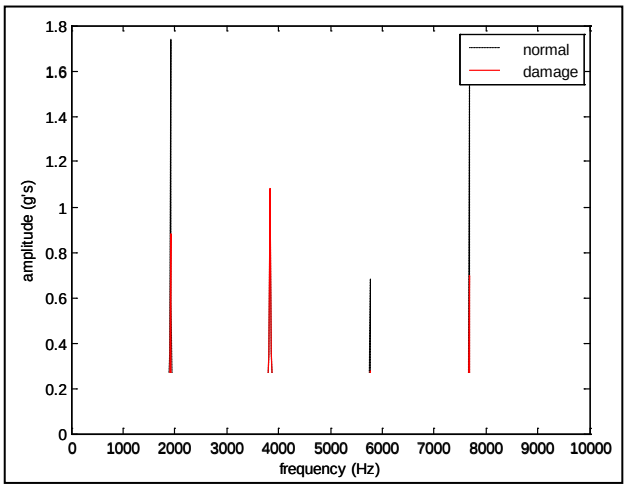

Figure 10. Frequency spectrum comparison.

This utility of this metric is demonstrated in figure 11. The FE2 was calculated using the FFT data points from the two curves in figure 10. Comparing the FE2 metric of figure 11 with the kurtosis parameter of figure 9, FE2 provides a much stronger indication for this particular damage condition. However, this may not always be the case. Further investigation and calibration of the FE2 threshold is required.

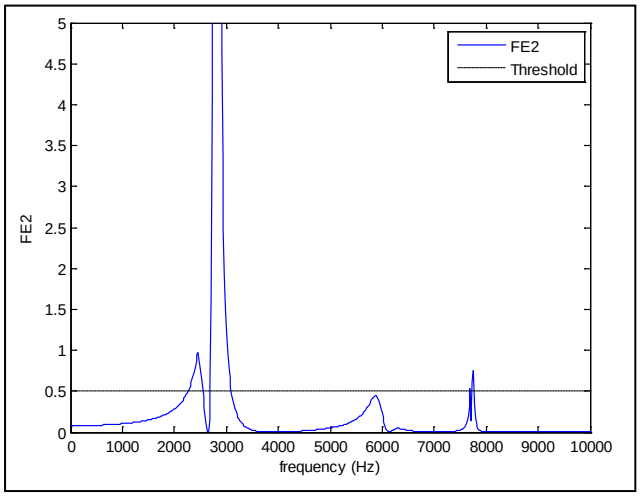

Figure 11. FE2 diagnostic parameter.

7. Additional Considerations

The worn condition presented here did not seem to indicate a drastic fault condition, which leads to a discussion on the different levels of damage. This implies that some *a priori* knowledge is

required on the differences between light, intermediate, and severe fault levels and how to model each of them. This may not be necessary in more distinct faults such as pitting, spalling, cracking, etc., where the defect has a more pronounced signature. A more severe wear condition may produce a more drastic result.

Another consideration is the ability to determine a standard fault signature for a given condition. These signatures will most likely be statistical or "average" patterns, requiring several iterations of testing and modeling scenarios to establish, which leads to the third consideration. The damage thresholds of the diagnostic parameters, especially the FE2 parameter, require calibration to ensure accuracy.

Finally, the instrumentation dynamics associated with epicyclic gear vibration must be addressed. An accelerometer attached to the casing near the ring gear measures the vibration of the epicyclic gear train. As each planet passes the accelerometer during a rotation, the sensor detects an increase in the vibration level. Thus, for *n* planets, a *n*/rev amplitude modulation is produced. The resulting measured vibration signal is therefore a convolution of the actual vibration of the gear set and the modulation caused by the planets moving past the accelerometer. The current model does not capture this effect.

8. Conclusions

This report has presented the results of a preliminary study into the feasibility of using a physics-based helicopter transmission model as a method of fault prediction and detection in support of CBM initiatives. Two simulations, one each for normal and damage operating conditions were presented using a lumped parameter, finite element model. The time and frequency domain responses were calculated for each and compared. Damage detection was illustrated using both a traditional diagnostic parameter and a new frequency-based parameter, FE2, although several iterations of testing and simulation are required to establish new parameter thresholds. The model itself requires further development and testing, to include sensitivity studies, to ensure a valid representation of the system dynamics.

Maturity of this technology will result in increased accuracy and confidence in fault detection and diagnosis, characterized by higher detection rates and fewer false alarms. It can serve as the foundation for incorporating transmission models into vibration and health monitoring systems, provide predictive capability prior to testing, and provide a useful tool for testing and evaluating condition indicator effectiveness.

From a CBM standpoint, this type of technology can aid in improving operational readiness, cost savings, and maintenance downtime.

9. References

1. Harris, F.; Kasper, E.; Iseler, L. *U.S. Civil Rotorcraft Accidents, 1963 through 1997*; NASA TM 2000-209597, USAAMCOM TR-00-A-006; 2000.

2. Aviation Accident Investigation Board (U.K.), Initial Accident Report EW/C2009/04/01, 2009.

3. Samuel, P.; Pines, D. A Review of Vibration-Based Techniques for Helicopter Transmission Diagnostics. *Journal of Sound and Vibration* **2005**, *282*, 475–508.

4. Lebold, M.; McClintic, K.; Campbell, R.; Byington, C.; Maynard, K. Review of Vibration Analysis Methods for Gearbox Diagnostics and Prognostics. *Proceedings of the 54th Meeting of the Society for Machinery Failure Prevention Technology*, MFPT, Haymarket, VA, 2000, 623–634.

5. Khanmohammedi, S.; Alizadeh, G.; Giasi, A. Stochastic Modeling of Gearbox via Genetic Algorithm. *Proceedings of the 15th IASTED International Conference*, edited by M. Hamza, IASTED, Calgary, Alberta, 2006, 484–488.

6. Zakrajsek, J.; Townsend, D.; Decker, H. An Analysis of Gear Fault Detection Methods as Applied to Pitting Fatigue Failure Data. *Proceedings of the 47th Meeting of the Mechanical Prevention Group*, Compiled by H. Pusey and S. Pusey, Vibrational Institute, Willowbrook, IL, 1993, 199–208.

7. Garga, A.; Elverson, B.; Lang, D. Fault Classification in Helicopter Vibration Signals. *Proceedings of the American Helicopter Society 53rd Annual Forum*, AHS, Alexandria, VA, 1997, 1316–1323.

8. Swansson, N. Application of Vibration Signal Analysis Techniques to Signal Monitoring. *Proceedings of the Conference on Lubrication, Friction, and Wear in Engineering 1980*. Barton, ACT; Institution of Engineers, Melbourne, Australia, 1980, 262–267.

9. Dykas, B.; Krantz, T.; Decker, H.; Lewicki, D. Experimental Determination of AH-64 Apache Tailshaft Hanger Bearing Vibration Characteristics with Seeded Faults. *Proceedings of the American Helicopter Society 65th Annual Forum on Disc* [CD-ROM], AHS, Alexandria, VA, 2009.

10. Lewicki, D.; Coy, J. *Vibration Characteristics of OH-58A Helicopter Main Rotor System*; NASA TP-2705, ARL TR-86-C-42; 1987.

11. Keller, J.; Grabill, P. Vibration Monitoring of UH-60A Main Transmission Planetary Carrier Fault. *Proceedings of the American Helicopter Society 59th Annual Forum on Disc* [CD-ROM], AHS, Alexandria, VA, 2003.

12. Dempsey, P.; Handschuh, R.; Afjeh, A. *Spiral Bevel Damage Detection Using Decision Fusion Analysis*; NASA TM-2002-211814, ARL-TR-2744; 2002.

13. Schwartz, B.; Jones, D. Quadratic and Instantaneous Frequency Analysis of Helicopter Gearbox Faults. *Mechanical Systems and Signals Processing* **2000**, *14* (4), 579–595.

14. Dempsey, P.; Keller, J.; Wade, D. Signal Detection Theory Applied to Helicopter Transmission Diagnostic Thresholds. *Proceedings of the American Helicopter Society 65th Annual Forum on Disc* [CD-ROM], AHS, Alexandria, VA, 2009.

15. Dempsey, P.; Lewicki, D.; Decker, H. *Investigation of Gear and Bearing Fatigue Damage Using Debris Particle Distribution*; NASA TM 2004-212883, ARL-TR-3133; 2004.

16. Dempsey, P.; Lewicki, D.; Decker, H. *Transmission Bearing Damage Detection Using Decision Fusion Analysis*; NASA TM 2004-213382, ARL-TR-3328; 2004.

17. Hess, A.; Hardman, W. Seeded Fault Testing in Support of Mechanical Systems Prognostic Development. *Aerospace Conference 2002 Proceedings*, Vol. 6, IEEE, Washington, D.C., 2002, 2995–3004.

18. Blunt, D.; Keller, J. Detection of a Fatigue Crack in a UH-60A Planet Gear Carrier Using Vibration Analysis. *Mechanical Systems and Signals Processing* **2006**, *20*, 2095–2111.

19. Wu, S.; Zuo, M.; Parey, A. Simulation of Spur Gear Dynamics and Estimation of Fault Growth. *Journal of Sound and Vibration* **2008**, *317*, 608–624.

20. McFadden, P. Detecting Fatigue Cracks in Gears by Amplitude and Phase Demodulation of the Meshing Vibration. *Journal of Vibration, Acoustics, Stress, and Reliability in Design* **1986**, *108*, 165–169.

21. Lewicki, D.; Dempsey, P.; Heath, G.; Shanthakumaran, P. Quantification of Condition Indicator Performance on a Split Torque Gearbox. *Proceedings of the American Helicopter Society 65th Annual Forum on Disc* [CD-ROM], AHS, Alexandria, VA, 2009.

22 Choy, F.; Polyshchuk, V.; Zakrajsek, J.; Handschuh, R.; Townsend, D. Analysis of the Effects of Surface Pitting and Wear on the Vibrations of a Gear Transmission System. *Tribology International* **1996**, *29* (1), 77–83.

23 Flodin, A.; Andersson, S. Simulation of Mild Wear in Spur Gears. *Wear* **1997**, *207*, 16–23.

24. Krantz, T.; Oswald, F.; Handschuh, R. *Wear of Spur Gears Having a Dithering Motion and Lubricated with a Perflourinated Polyether Grease*; NASA TM 2007-215008, ARL TR-4124; 2007.

25. Kuang, J.; Lin, A. The Effect of Tooth Wear on the Vibration Spectrum of a Spur Gear Pair. *Journal of Vibration and Acoustics* **2001**, *123*, 311–317.

26. Ma, J.; Li, C. On Localized Gear Defect Detection by Demodulation of Vibrations - A Comparision Study. *Manufacturing Science & Engineering Division, Proc. ASME 1995 Int. Mech. Engr. Congress and Exposition* **1995**, *2* (1), 565–576.

27. Forrester, B. A Method for the Separation of Epicyclic Planet Gear Vibration Signatures. *Proceedings of the 3rd International Conference on Acoustical and Vibration Surveillance Methods and Diagnostic Techniques*, 1998, 539–547.

28. Wang, W.; McFadden, P. Early Detection of Gear Failure by Vibration Analysis I. Calculation of the Time-Frequency Distribution. *Mechanical Systems and Signals Processing* **1993**, *7* (3), 193–203.

29. Wang, W.; McFadden, P. Early Detection of Gear Failure by Vibration Analysis II. Interpretation of the Time-Frequency Distribution Using Image Processing Techniques. *Mechanical Systems and Signals Processing* **1993**, *7* (3), 205–215.

30. Barry, D. Fast Calculation of the Choi-Williams Time-Frequency Distribution. *IEEE Transactions on Signal Processing* **1992**, *40* (2), 450–454.

31. Trendafilova, I. Vibration-Based Damage Detection in Structures Using Time Series Analysis. *Journal of Mechanical Engineering Science* **2006**, *223* (3), 261–272.

32. Ma, J.; Li, C. Gear Defect Detection Through Model Based Wideband Demodulation of Vibrations. *Mechanical Systems and Signals Processing* **1996**, *10* (5), 653–665.

33. McFadden, P.; Smith, J. An Explanation for the Asymmetry of the Modulation Sidebands About the Tooth Meshing Frequency in Epicyclic Gear Vibration. *Proceedings of the Institution of Mechanical Engineers, Part C*, Vol. 199, No. 1, 65–70.

34. McFadden, P.; Smith, J. A Signal Processing Technique for Detecting Local Defects in a Gear from the Signal Average of the Vibration. *Proceedings of the Institution of Mechanical Engineers, Part C*, Vol. 199, No. 4, 287–292.

35. Wu, B.; Saxena, A.; Patrick, R.; Vachtsevanos, G. Vibration Monitoring for Fault Diagnosis of Helicopter Planetary Gears. *Proceedings of the 16th IFAC World Congress on Disc* [CD-ROM], IFAC, Laxenburg, Austria, 2005.

36. Özgüven, H.; Houser, D. Mathematical Models Used in Gear Dynamics. *Journal of Sound and Vibration* **1988**, *121*, 383–411.

37. Blankenship, G.; Singh, R. A Comparative Study of Selected Gear Mesh Interface Dynamic Models. *Proceedings of the 6th International Power Transmission and Gearing Conference, ASME*, New York, NY, 1992, 137–146.

38. Choy, F.; Townsend, D.; Oswald, F. *Dynamic Analysis of Multimesh-Gear Helicopter Transmissions*; NASA TP-2789; 1988.

39. McFadden, P. Examination of a Technique for the Early Detection of Failure in Gears by Signal Processing of the Time Domain Average of the Meshing Vibration. *Mechanical Systems and Signals Processing* **1987**, *1* (2), 173–183.

40. Dickey, Beth. NASA Announces Pennsylvania Aeronautics Research Awards. 25 Nov 2008, NASA Press Release 08-312e.

41. Stringer, D. Geared Rotor Dynamic Methodologies for Advancing Prognostic Modeling Capabilities in Rotary-Wing Transmission Systems. Ph.D. Dissertation, Mechanical and Aerospace Engineering Dept., University of Virginia, Charlottesville, VA, 2008.

42. Yoon, K. The Combined Mesh Stiffness Characteristics of Straight and Spiral Bevel Gears. Master's thesis, North Carolina State University, Mechanical Engineering Dept., 1989.

43. Stringer, D.; Sheth, P.; Allaire, P. Gear Modeling Methodologies for Advancing Prognostic Capabilities in Rotary-Wing Transmission Systems. *Proceedings of the American Helicopter Society 64th Annual Forum on Disc* [CD-ROM], AHS, Alexandria, VA, 2009.

44. Litvin, F. *Theory of Gearing*; NASA RP-1212, AVSCOM TR 88-C-035, 1989.

45. Lin, J.; Parker, R. Analytical Characterization of the Unique Properties of Planetary Gear Free Vibration. *Journal of Vibration and Acoustics* **1999**, *121*, 316–321.

46. Parker, R.; Lin, J. *Modeling, Modal Properties, and Mesh Stiffness Variation Instabilities of Planetary Gears*; NASA CR 2001-210939, ARL-CR-462; 2001.

47. Mobley, R. An Introduction to Predictive Maintenance, 2nd ed.; Butterworth Heinemann: New York, 2002, pp. 306–309.

48. Mitchell, L.; Mellen, D. *Torsional-Lateral Coupling in a Geared, High-Speed Rotor System*; ASME Paper 75-DET-75; 1975.

INTENTIONALLY LEFT BLANK.

Appendix. Nomenclature

a_n,b_n	=	Fourier coefficients
b	=	subscript, spiral-bevel gear pair
[**C**]	=	general damping matrix
{**F**(t)}	=	force and moment vector
[**G**]	=	gyroscopic matrix
i, j	=	indices
j	=	imaginary component
[**K**]	=	stiffness matrix
k_{mesh}	=	mesh stiffness
[**M**]	=	mass matrix
NT	=	number of gear teeth
n	=	number of planets; n^{th} harmonic
{**q**}	=	generalized displacement vector
sb	=	subscript, sideband
{**T**}	=	torque vector
t	=	time
Ω	=	rotational speed

No. of Copies	Organization
1	ADMNSTR ELEC DEFNS TECHL INFO CTR ATTN DTIC OCP 8725 JOHN J KINGMAN RD STE 0944 FT BELVOIR VA 22060-6218
1	DARPA ATTN IXO S WELBY 3701 N FAIRFAX DR ARLINGTON VA 22203-1714
1 CD	OFC OF THE SECY OF DEFNS ATTN ODDRE (R&AT) THE PENTAGON WASHINGTON DC 20301-3080
1	US ARMY RSRCH DEV AND ENGRG CMND ARMAMENT RSRCH DEV AND ENGRG CTR ARMAMENT ENGRG AND TECHNLGY CTR ATTN AMSRD AAR AEF T J MATTS BLDG 305 ABERDEEN PROVING GROUND MD 21005-5001
1	US ARMY TRADOC BATTLE LAB INTEGRATION & TECHL DIRCTRT ATTN ATCD B 10 WHISTLER LANE FT MONROE VA 23651-5850
1	PM TIMS, PROFILER (MMS-P) AN/TMQ-52 ATTN B GRIFFIES BUILDING 563 FT MONMOUTH NJ 07703
1	US ARMY INFO SYS ENGRG CMND ATTN AMSEL IE TD F JENIA FT HUACHUCA AZ 85613-5300
1	COMMANDER US ARMY RDECOM ATTN AMSRD AMR W C MCCORKLE 5400 FOWLER RD REDSTONE ARSENAL AL 35898-5000

No. of Copies	Organization
3	NASA GLENN ATTN RDRL-VT D STRINGER 21000 BROOK PARK RD MS 23-3 CLEVELAND OH 44135-3191
1	US GOVERNMENT PRINT OFF DEPOSITORY RECEIVING SECTION ATTN MAIL STOP IDAD J TATE 732 NORTH CAPITOL ST NW WASHINGTON DC 20402
1	US ARMY RSRCH LAB ATTN RDRL CIM G TECHL LIB T LANDFRIED BLDG 4600 ABERDEEN PROVING GROUND MD 21005-5066
3	US ARMY RSRCH LAB ATTN RDRL CIM P TECHL PUB ATTN RDRL CIM L TECHL LIB ATTN IMNE ALC IMS MAIL & RECORDS MGMT ADELPHI MD 20783-1197
3	UNIVERSITY OF VIRGINIA DEPT OF MECH & AERO ENGR ATTN P ALLAIRE PO BOX 400746 MECH. ENGR. BLDG 208-B CHARLOTTESVILLE VA 22904
TOTAL:	19 (17 HCS, 1 CD, 1 PDF)